



# The distance potential function-based finite-discrete element method

Xunnan Liu<sup>1</sup> · Jia Mao<sup>1</sup> · Lanhao Zhao<sup>1</sup> · Linyu Shao<sup>1</sup> · Tongchun Li<sup>1,2</sup>

Received: 23 November 2019 / Accepted: 17 August 2020 / Published online: 8 September 2020  
© Springer-Verlag GmbH Germany, part of Springer Nature 2020

## Abstract

The work is devoted to a coupling method for the finite element method (FEM) and the distance potential discrete element method. In this work, a well-defined distance potential function is developed. Meanwhile, a holonomic and precise algorithm for contact interaction is established, accounting for the influence of the tangential contact force. In addition, the measurement of deformation behaviors of each discrete element is handled by the FEM, where the coupling model and the conversion method of the equivalent nodal force accounting for the influence of contact forces are proposed to generate the corresponding equations of motion. Finally, the velocity verlet algorithm is applied enabling the significant simplification for the calculation of the equations of motion. The proposed approach provides an accurate contact interaction avoiding the influence of the element shape and reflect the movement procedure of multiple deformable bodies precisely. This viewpoint is proved by the classical benchmark cases.

**Keywords** Discrete element method · Finite element method · Distance potential function · Contact force model · Deformation behaviors

## 1 Introduction

The discrete element method (DEM) offers an efficient tool for tracing mechanical behaviors of discontinuous media. Initially, the underlying rigid-body assumption is adopted in the DEM. This assertion shows its rationality for the systems, such as joined rock masses and block collections, since the deformation of such media is mainly caused by the sliding and rotation of blocks and evolution of discontinuous interfaces. However, the system consisted of multiple deformable bodies usually involves with the large displacement and rotation, and investigations conducted in these phenomena gain more popularity in typical applications of the computational mechanics [1, 2]. Accordingly, a model capable of representing the interactions and the deformation properties is extremely indispensable for modeling the complicated behaviors of the discontinuous system.

In recent times, an increasing number of models are set up by coupling the DEM with continuous approaches to capture the actual behavior of the system associated with geometric information and contact mechanical properties. A typical simplified model is suggested by Cundall and Strack [3–5]. The main idea refers to the idealized discontinuous mathematical model, that deformable blocks are represented by the triangular elements and joints are modelled as contact surfaces between different blocks [6]. On the basis, the finite difference method is applied to consider the deformability. The normal and tangential contact springs are adopted as a reasonable mathematical representations of the contact physics [4, 5]. As a result, different mathematical models, such as point-to-point, point-to-edge, and edge-to-edge, are not robust and generally very complex, but are necessarily according to the different contact situations [7, 8]. Furthermore, due to the non-determinacy of the normal contact force at a corner, it cannot deal with the point-to-point contact state. This also results in an inconsistent contact force, which can cause energy imbalance and numerical errors. One common practice to overcome the corner singularity is to employ a corner rounding procedure, so that blocks can slide past one another in a smooth way [9]. Nevertheless, this practice has a negative effect on the accuracy and robustness.

The combined finite-discrete element method (FDEM), developed by Munjiza and Owen [10], makes a revolutionary

✉ Lanhao Zhao  
zhaolanhao@hhu.edu.cn

<sup>1</sup> College of Water Conservancy and Hydropower Engineering, Hohai University, Nanjing Xikang Rd., 210098, People's Republic of China

<sup>2</sup> College of Agricultural Engineering, Hohai University, Nanjing 210098, People's Republic of China

change on the model of contact interaction. Entirely different from the standard DEM, the FDEM defines a potential function with the area calibration function. The distance penetration applied in the standard DEM is represented by the overlapping area. Accordingly, the contact interaction is performed by the distributed contact force instead of the central contact force, hence the calculation of contact forces in the FDEM becomes convenient and uniform by an integral of the potential function on the embedded area without discussions of different contact situations completely, whilst the energy conservation and momentum balance properties are preserved. Furthermore, each discrete block is defined by a continuum mesh of finite element zones, with each zone behaving according to a prescribed linear or nonlinear stress–strain law. Meanwhile, the No Binary Search (NBS) method [11], which is noted for its linear properties for the contact detection both in dense and loose packs of blocks, is developed to reduce the CPU requirement of contact problems and improve the efficiency [12].

The FDEM still suffers from some deficiencies, even though diverse applications have been carried out to validate the performance of this approach [13–18]. As the potential function in the FDEM is defined as the normalized penetrated area, the potential magnitude is not identical at all time even with a same penetration and overlapping area in a same element. Consequently, the contact interaction may undergo deviations [19]. The principal reason for this phenomenon fundamentally boils down to the inherent deficiency of the potential definition, which lacks a clear physical meaning and a measurement for the penetration between contact elements [20]. Besides, the numerical model does not indicate the influence of the tangential contact force [7]. Another severe drawback is that this potential function has a strict restriction on the element type and cannot be applied in an arbitrary polygonal element [12]. Moreover, the stress and strain inside the discrete elements are assumed constant, as the linear triangular finite elements, e.g. the first-order elements, have disadvantages of the corresponding theoretical formulation. Even though the higher-order interpolation functions for the triangular elements have been combined with other approaches to address the shortcomings of their constant strain counterparts [21], its implementation is still limited, due to the high cost in the computational resources.

In order to overcome the presented disadvantages, a distance potential function-based FEM-DEM method is proposed in this work. The basic idea of the proposed method is motivated by the limitations of the FDEM owing to the intrinsic defects of the potential function, the omission of the tangential force, and the low accuracy for characterizing the stress and deformation behaviors. Furthermore, the displacement interpolation function, the stiffness matrix, and the integration algorithm of load vector for polygonal elements have been developed [22], which make it possible to

directly calculate the stress and strain of complex elements. In this approach, a novel definition of distance potential function is developed relying on the defined distance calibration function, and a complete calculation of the normal contact interaction is performed as an integration of this distance potential function on the boundaries of the overlapping area. The proposed method also provides a precise definition of the tangential direction and the computational algorithm. In addition, the coupling model of the presented method and the conversion method of the equivalent nodal force for the uncoupled contact interaction from the equations of motion are applied. Finally, the typical combination of the distance potential function based DEM and the finite element formulation is presented together with the velocity verlet method [23]. The new distance potential function is based on the normalized penetrated distance. In comparison with the definition in the FDEM, this distance potential function exhibits a clear physical meaning and presents an accurate measurement of penetration for the contact elements. Accordingly, both the magnitude of the distance potential function and numerical solution of the contact interaction are calculated regardless of the element shapes. Moreover, a much wider range of choices for the finite element types, for instance the four-node quadrilateral element, which has been driven to improve the computational accuracy of the stress and deformation, are available, due to the extension of the element shapes.

This paper is organized as follows. The motivation and methodology are illustrated in Sect. 2, including the main issues existed in the FDEM and the counterplans in this paper, followed by mathematical models of the discrete element method in which the distance potential function and the algorithm of contact interactions are provided in Sect. 3. Then the numerical model of the distance potential-based FEM-DEM method is discussed in Sect. 4. Subsequently, several illustrative verifications are reported to validate the presented method in Sect. 5. At the end of this paper, conclusions are provided in Sect. 6.

## 2 Motivation

### 2.1 Basic idea of the FDEM

As described in the FDEM [12], the discrete element is discretized with a mesh consisting of triangular finite elements. Each employed finite element mesh captures the deformability of a single discrete element.

The contact detection algorithm, namely the NBS method [11], then is applied in this case for an investigation of all the finite element pairs in contact. Subsequently, the contact interaction is based on the assumption that the contact triangular elements,  $\beta_t$  and  $\beta_c$ , penetrate each other, resulting in

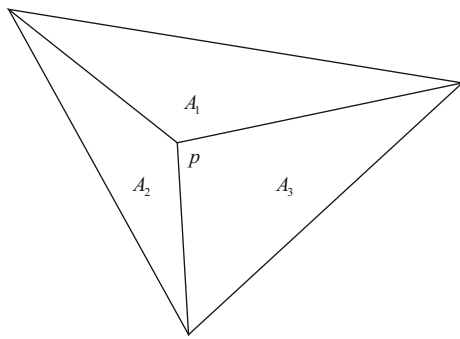


**Fig. 1** The sub-triangles divided by the point  $p$

a distributed normal contact force  $f_n$ . It is associated with the shape and size of the overlapping area, and the detail formulation is given as

$$f_n = k_n \oint_{\Gamma} n_{\Gamma} (\varphi_c - \varphi_t) d\Gamma, \tag{1}$$

where  $\varphi_c$  and  $\varphi_t$  are the potential function at the point in  $\beta_t$  and  $\beta_c$ , respectively,  $\Gamma$  is the boundary of the overlapping area,  $n_{\Gamma}$  is the outward unit normal vector of  $\Gamma$ , and  $k_n$  is the normal stiffness.

Value of this potential function of the point in the element is defined as

$$\varphi = \min \left\{ \frac{3A_1}{A}, \frac{3A_2}{A}, \frac{3A_3}{A} \right\}, \tag{2}$$

where  $A_i$ ,  $i = 1, 2, 3$  is the area of the corresponding sub-triangles, as shown in Fig. 1, and  $A$  represents the area of the element.

The computed contact force is applied together with all other forces to the simulated body, and the central difference method (CDM) is adopted to solve the equation of motion [24]

$$M\ddot{u} + C\dot{u} + f_{int} = f_{ext} + f_c, \tag{3}$$

where  $M$  and  $C$  are the mass matrix and the damping diagonal matrix, respectively,  $\dot{u}$  and  $\ddot{u}$  are the vectors of velocity, and acceleration, respectively,  $f_{int}$ ,  $f_{ext}$  and  $f_c$  are the equivalent nodal force vectors contributed by the deformation of the element, the external force, and the contact force between the contact finite elements.

Finally, the strain and stress distributions in the deformable body are evaluated from the computed displacement of each body.

## 2.2 Some issues in the FDEM

The FDEM exhibits a completely unified contact model for various contact types and provides a feasible coupling way

for the DEM and the FEM to measure the deformation behavior of discrete blocks. However, there are still three critical problems listed as follows, when it is applied to solve the contact interaction between the deformable polygonal blocks.

1. The potential function is defined for the regular triangular element, and it cannot be applied in the arbitrary triangular element. As described in Eq. (2), the potential function is a function of dimensionless embedding area, and itself provides a measurement of the embeddedness between the contact elements. Accordingly, points with a same penetration in the same element ought to have the same potential value. Nevertheless, the potential value is commonly determined associated on the geometrical features of the element. As shown in Fig. 2, the distribution of the potential value is exhibited, and three points,  $p_1$ ,  $p_2$ , and  $p_3$  with a same penetration distance are selected. However, high differences are indicated in every point in Fig. 2a. The potential values of the points are given by Eq. (2) according to the area of the corresponding sub-triangles as illustrated in Fig. 2b. Because the lengths of the boundaries of the element are not equivalent,  $\varphi(p_1) \neq \varphi(p_2) \neq \varphi(p_3)$ , even the same penetration distance for each point in the same element. The size-effect of the boundaries of the element can be observed clearly.
2. The smooth deficiency of the potential function in the polygonal element. Figure 3 exhibits the distribution of the potential magnitude in an arbitrary quadrilateral element. The presence of discontinuities along the interfaces can be observed from the illustration. It presents a strict restriction of the potential function to the element type and cannot be used to compute the contact interaction between polygonal elements.
3. The accuracy loss in the description of the stress and strain distribution in the element. For a variety of reasons, the FDEM is based on the triangular finite element. The first-order element has both the advantages and disadvantages of the corresponding theoretical formulations. Although in many cases they are capable of producing good results, they cannot reflect the distribution of the stress and strain inside the element.

## 2.3 The proposed deformable distance potential discrete element method

As the kind of numerical errors mainly come from the potential definition, a reasonable and generalized definition of a potential function for the arbitrary polygonal elements becomes the key issue. The potential function ought to be defined as signed distance function and itself provides an exact measurement of the embeddedness between the contact elements. It is a straightforward choice to establish the

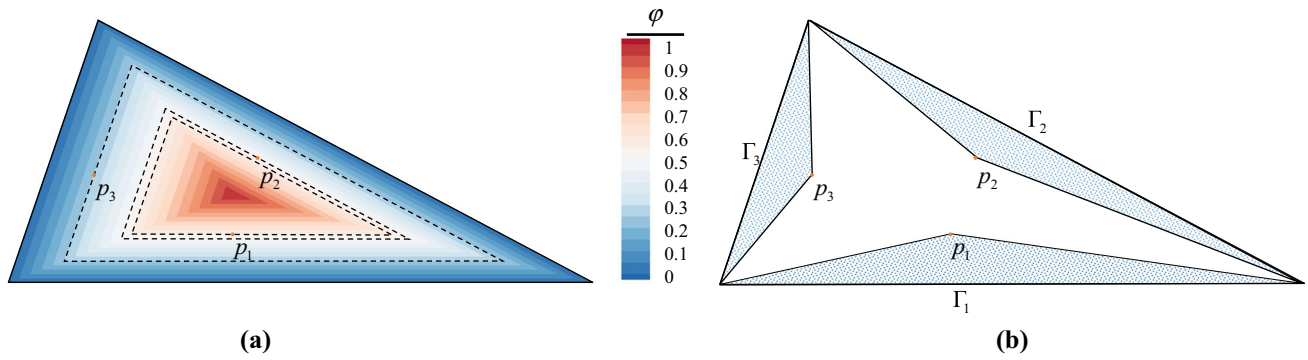


**Fig. 2** The potential distribution in triangular elements shown in (a), and three points  $p_1$ ,  $p_2$ , and  $p_3$  with a same penetration shown in (b)

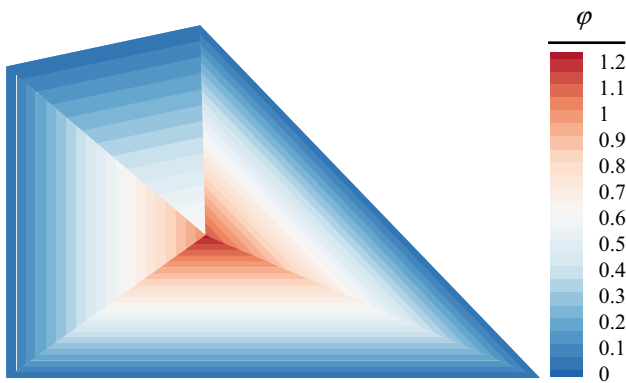


**Fig. 3** The distribution of the potential magnitude in an arbitrary quadrilateral element

potential function according to the penetration distance. In this way, points with the same penetrated distance have the same potential magnitude within the same element.

In this case, a distance calibration function is adopted, and the potential function is described as a dimensionless distance function, namely the distance potential function. The distance potential distributions with a constant gradient in varied blocks are presented in Fig. 4. It is worthwhile to notice that distance potential value is achieved without influence of the element shape. Moreover, it can be used in the arbitrary polygonal elements. Consequently, the high-

accuracy element, e.g. the convex polygonal element [22], is employed to provide the precise deformation characteristics of the simulated body. As a result, it can avoid errors in the calculation of both potential and normal contact force as discussed in Sect. 2.2. The solution process of different types of elements is basically the same, so this article uses four-node quadrilateral elements as an example to explain in detail.

### 3 Mathematic model of distance potential discrete element method

In this section, mathematic models of contact forces in the presented method are illustrated. Quadrilateral blocks, discretized with a quadrilateral finite element respectively, are selected to account for the computing process.

In this work, the model is established in accordance with the energy conservation [25]. Assuming the contact elements,  $\beta_c$  and  $\beta_t$ , move along any closed path  $L$ , the total work  $W$  produced by the normal contact force can be expressed as

$$W = \oint_L f_n dL, \tag{4}$$

Apparently,  $W$  satisfies  $W = 0$ , when the contact is elastic. In consequence,  $f_n$  has to be potential vector, and it can be

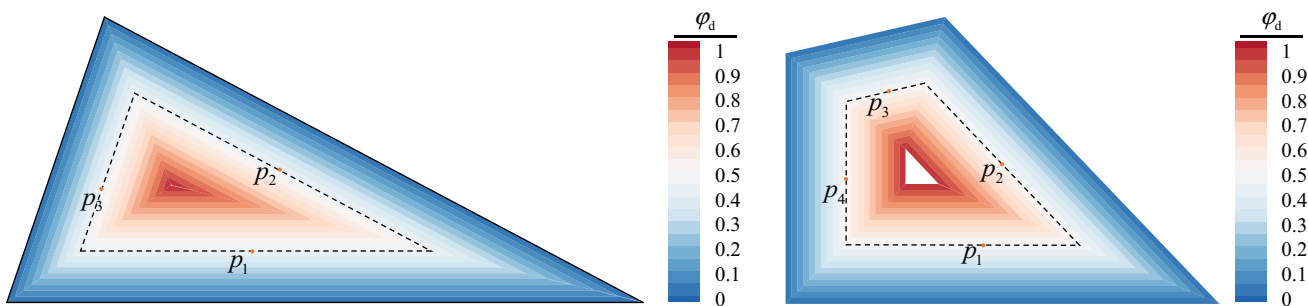


**Fig. 4** The distance potential distribution in varied elements

expressed as the negative value of the gradient of the scalar function (potential function)

$$f_n = -k_n \nabla \varphi \tag{5}$$

### 3.1 The distance potential discrete element method

The most notable difference between the distance potential discrete element method and the FDEM lies in the choice of the potential function in Eq. (5). Instead of the area calibration function as described in Eq. (2), this newly presented method employs the radius of the maximal inscribed circle of the element,  $r$ , and a novel distance potential function  $\varphi_d$  is defined as

$$\varphi_d = \frac{1}{r} \min\{h_i\}, \quad \varphi_d \leq 1, \tag{6}$$

where  $h_i$  stands for the distance between the point inside the element and each boundary of the element. The distribution of the distance potential function in the arbitrary quadrilateral element is shown in Fig. 5.

Due to the arbitrary element shapes, the definition of the distance potential function results in an internal polygonal area, namely the singular area, surrounded by a set of points with a same distance  $r$  to the corresponding boundary, as shown in Fig. 5a. It can be obtained geometrically by translating the nodes along the angle bisector of the element as illustrated in Fig. 5b. Points in the singular area are not defined by the distance potential function. In accordance with the basic assumption of the DEM, the penetration will not happen in this area, due to the large value of the normal contact stiffness. Consequently, the singular area is not of significance for the solution procedure.

The distance potential value is equal to 1 on the boundaries of the singular area, and 0 on the bases of the element. The strong smoothness deficiency and nonlinear distribution of the distance potential function exhibited in Fig. 5a. Nevertheless, the element is discretized into sub-polygonal blocks by the angle bisectors, as shown in Fig. 5c, in which the invariable gradient and a linear distribution of the distance potential function are achieved.

By introducing the Eqs. (1) (5) and (6), the normal contact force between the contact pairs  $\beta_c$  and  $\beta_t$ , as shown in Fig. 6a, can be described as an integration of the distance potential function over the boundaries of the overlapping area

$$f_n = \sum_{i=1}^{N_\Gamma} \left\{ n_{i,n} k_n \int_{\Gamma_i} [\varphi_{d,c} - \varphi_{d,t}] d\Gamma_i \right\}, \tag{7}$$

where  $\varphi_{d,c}$  and  $\varphi_{d,t}$  are the value of distance potential function belonging to the blocks  $\beta_c$  and  $\beta_t$  respectively,  $n_{i,n}$  is the outward unit normal vector of the boundary  $\Gamma_i$ ,  $k_n$  represents the normal contact stiffness according to the definition by

Munjiza, and  $N_\Gamma$  stands for the number of the boundaries of the overlapping area.

A local coordinate system given by  $(v, v)$  is introduced to minimize the necessary numerical operations. Figure 6b shows the local coordinate system established on edge  $\Gamma_1$ . Distribution of the distance potential value between the interaction points, e.g.  $p_i, i = 1, \dots, 4$  shown in Fig. 6b, is along the straight line and linear. Consequently, Eq. (7) is simplified as

$$f_n = k_n \sum_{i=1}^{N_\Gamma} n_{i,n} \sum_{j=1}^{N_{int}} \frac{1}{2} \left\{ [\varphi_{d,c}(p_j) + \varphi_{d,c}(p_{j+1})] - [\varphi_{d,t}(p_j) + \varphi_{d,t}(p_{j+1})] \right\} l_{p_j p_{j+1}}, \tag{8}$$

where  $l_{p_j p_{j+1}}$  is the distance between the interaction points  $p_j$  and  $p_{j+1}$ , and  $N_{int}$  is the total number of the interaction points.

### 3.2 Tangential contact interaction algorithm

Due to the ambiguity of the tangential direction and omission of the influence from the tangential contact force, the FDEM often introduces an inevitable numerical error into the computation, which may cause an enormous distortion or a total simulation failure. Thus, the determination method for the tangential contact force is necessary for a precise simulation result. In the standard method [20], the tangential force associated with the tangential incremental displacement at time  $t + \Delta t$

$${}^{t+\Delta t} f_s = \sum_{j=1}^{N_s} ({}^t f_s + k_s \Delta \delta_s)_j, \tag{9}$$

is implemented as components on the boundaries of the block, where  ${}^{t+\Delta t} f_s$  and  ${}^t f_s$  are the tangential force at time  $t + \Delta t$  and  $t$ , respectively,  $k_s$  is the tangential contact stiffness,  $\Delta \delta_s$  is the tangential increment displacement of each boundary, and  $N_s$  is the total number of the boundaries.

The general expression, however, has a severe drawback with false tangential force. As shown in Fig. 7, block  $\beta_c$  impacts block  $\beta_t$  in a direction opposite that of  $y$  axis. Initially, blocks  $\beta_c$  and  $\beta_t$  are stacked in such way that they contact but there are no overlap and contact force between them. Then  $\beta_c$  is prescribed to move along the  $Y$  axis translationally only. The tangential forces  $f_{t,ac}$  and  $f_{t,ab}$ , along the entire path which can be obtained by Eq. (9). However, this is inconsistent with the physical intuition, because the relative tangential displacement increment is not occurred between the blocks. In addition, it can be observed that  $f_{t,ac}$  and  $f_{t,ab}$  have components along the normal direction, which affect the computation of the normal contact force. Otherwise an enormous computer memory (RAM) is necessary to record both



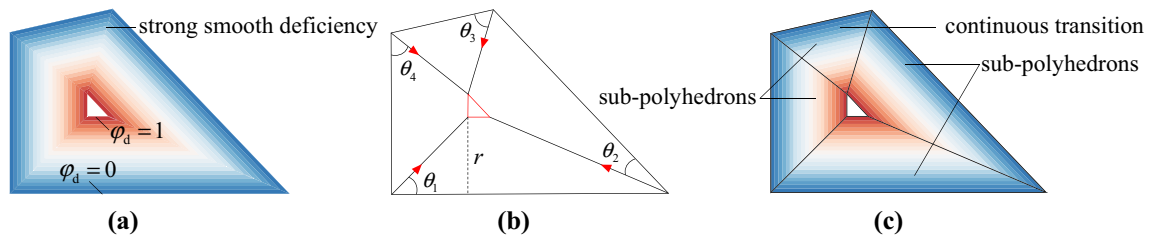


**Fig. 5** The distribution of the distance potential in a quadrilateral element shown in (a), the polyhedron divided into sub-polyhedral blocks shown in (b), and the invariable gradient and a linear distribution of the distance potential function in the sub-polyhedral blocks shown in (c)

**Fig. 6** Two contact polygonal blocks  $\beta_t$  and  $\beta_c$  and the normal contact force on edge  $\Gamma_1$

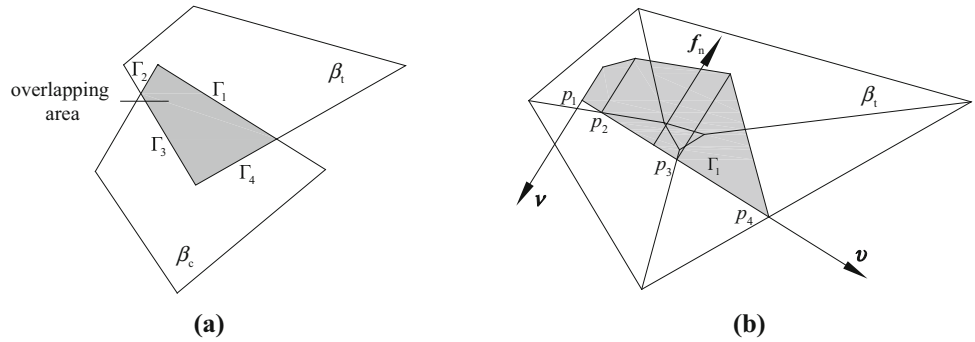
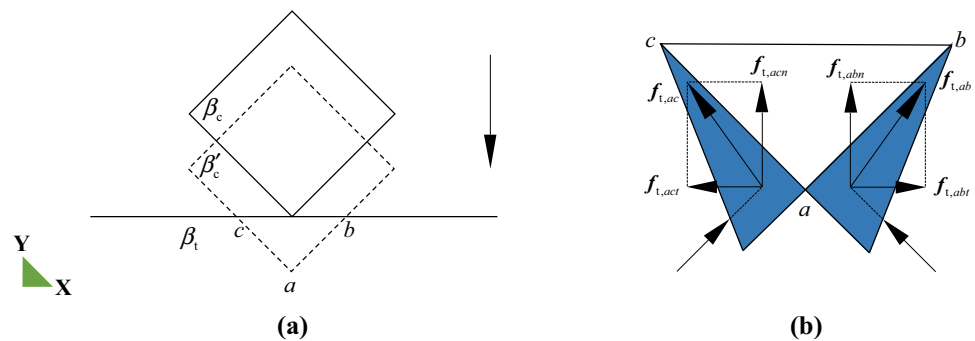


**Fig. 7** Tangential component of the block  $\beta_c$



the normal and tangential force and increment displacement at each time step for all boundaries of every block.

One possible way to remedy these deficiencies is that the calculation for tangential force is achieved by following the solution of the total normal contact force. The value of the tangential force is determined by the total tangential increment displacement, and the direction of the tangential force is perpendicular to the total normal contact force and the loading position is almost identical with the total normal contact force. Consequently, excessive computer memory requirements and the errors analyzed for the first method can be eliminated completely.

The relative velocity  $v$  of  $\beta_c$  to  $\beta_t$  is

$${}^{t+\Delta t}v = ({}^{t+\Delta t}\dot{u}_c - {}^{t+\Delta t}\dot{u}_t) + ({}^{t+\Delta t}\omega_c \times {}^{t+\Delta t}r_c - {}^{t+\Delta t}\omega_t \times {}^{t+\Delta t}r_t), \tag{10}$$

where  ${}^{t+\Delta t}\dot{u}_c$ ,  ${}^{t+\Delta t}\dot{u}_t$ ,  ${}^{t+\Delta t}\omega_c$  and  ${}^{t+\Delta t}\omega_t$  are the translational and angular velocities of blocks  $\beta_c$  and  $\beta_t$  at time  $t + \Delta t$ , respectively.

Then the incremental tangential displacement  $\Delta\delta_s$  is given by

$$\Delta\delta_s = \Delta\delta - (\Delta\delta \cdot \hat{n}_n) \cdot \hat{n}_n = [{}^{t+\Delta t}v - ({}^{t+\Delta t}v \cdot \hat{n}_n) \cdot \hat{n}_n] \Delta t, \tag{11}$$

where  $\Delta\delta$  is the incremental displacement between  $\beta_c$  and  $\beta_t$ , and  $\hat{n}_n$  is the unit direction vector of total normal contact force.

And the tangential contact force is obtained as

$${}^{t+\Delta t}f_s = {}^t f_s + k_s \Delta\delta_s, \tag{12}$$

It is highlighted, however, that the unit direction vector  $\hat{n}_n$  is updated every time step. In order to account for the direction of the tangential force, Eq. (12) must be corrected as

$${}^{t+\Delta t}f_s = R^t f_s + k_s \Delta\delta_s \tag{13}$$

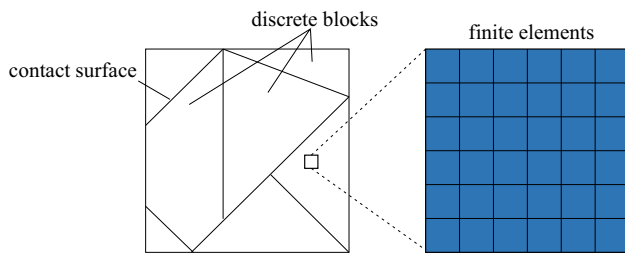


**Fig. 8** Numerical model of the distance potential function-based FEM-DEM method

where  $\mathbf{R}$  is the rotation matrix that rotates the normal vector at time  $t$  to the normal vector at time  $t + \Delta t$ .

The magnitude of the tangential contact force is checked with the Coulomb friction law relating to the total normal contact force  ${}^{t+\Delta t} \mathbf{f}_n$

$${}^{t+\Delta t} \mathbf{f}_s = \mathbf{n}_s \min(|{}^{t+\Delta t} \mathbf{f}_s|, \mu |{}^{t+\Delta t} \mathbf{f}_n|), \tag{14}$$

where  $\mu$  is the friction coefficient.

### 4 Numerical model of the distance potential function-based FEM-DEM method

In this section, the specific technologies used to accomplish the distance potential function-based FEM-DEM coupled method are illustrated. The coupling model is provided to deal with the contact relationship. Afterwards, the description of the equivalent nodal force of the contact force is illustrated. Finally, governing equations and the numerical scheme are established in an explicit way.

#### 4.1 Coupling model for the distance potential function-based FEM-DEM method

The developed model is shown in Fig. 8. The object in the computational domain is cut into discrete blocks of various shapes in terms of the internal discontinuous surfaces. The blocks are modeled by discrete elements, and the surfaces between the blocks are represented by the contact surfaces. Each discrete element is further discretized into four-node quadrilateral elements, as shown in Fig. 8.

Thus, the contact detection and the computing of the contact force are performed between the outermost finite elements, as shown in Fig. 9b. Then the contact force is assigned to the nodes of the contact finite elements according to the principle of static equivalence, which will be discussed in detail in Sect. 4.2. Therefore, the calculation of the contact force maintains a high degree of accuracy with complete consideration of the deformation of the block. However, it would bring about the enormous number of the contact detected elements and the rapid increment of computing time.

#### 4.2 The equivalent nodal force

Simulations of the deformable blocks is enabled by combining the DEM and FEM. In this case, the discrete blocks are discretized into the quadrilateral elements, as described in Fig. 9a, and calculations of contact interactions are performed among the contact finite elements, which are made distinct from other finite elements, as shown in Fig. 9b.

As mentioned above, the discrete blocks have been discretized into finite elements and the FEM is applied here to represent the deformation characteristics. Therefore, the conversion method of the equivalent nodal force for the contact force is extremely necessary for this problem. According to the principle of static equivalent [26], the contact forces on the nodes of the contact elements,  $\beta_c$  and  $\beta_t$ , as shown in Fig. 10, are given by

$$\mathbf{f}_{ci} = \mathbf{F}_c N_i, \tag{15}$$

where  $\mathbf{f}_{ci}$  stands for the equivalent nodal forces,  $N_i$  represents the shape functions, and  $\mathbf{F}_c$  is obtained as  $\mathbf{F}_c = \mathbf{f}_n + \mathbf{f}_s$ .

#### 4.3 Governing equations and the numerical scheme

Geometric nonlinearities, in this instance, including nonlinear aspects of deformation are arose from large displacements and large strains for each individual discrete element. The nonlinear finite element method is naturally adopted to address these nonlinear problems [27]. The node coordinates of the finite-element meshes describing the deformable discrete element is updated at each time step according to the governing equation (3). The time discretized formulation of the governing equation is shown as follows

$$\mathbf{M}{}^{t+\Delta t} \ddot{\mathbf{u}} + \mathbf{C}{}^{t+\Delta t} \dot{\mathbf{u}} + {}^{t+\Delta t} \mathbf{f}_{int} = {}^{t+\Delta t} \mathbf{f}_{ext} + {}^{t+\Delta t} \mathbf{f}_c \tag{16}$$

where  ${}^{t+\Delta t} \dot{\mathbf{u}}$  and  ${}^{t+\Delta t} \ddot{\mathbf{u}}$  are the vector of velocity, and acceleration at time  $t + \Delta t$ , respectively,  ${}^{t+\Delta t} \mathbf{f}_{int}$ ,  ${}^{t+\Delta t} \mathbf{f}_{ext}$  and  ${}^{t+\Delta t} \mathbf{f}_c$  represent the equivalent nodal force vectors due to the deformation of the element, the external force, and the contact force between the contact finite elements at time  $t + \Delta t$ .

Since the variables  ${}^{t+\Delta t} \dot{\mathbf{u}}$ ,  ${}^{t+\Delta t} \ddot{\mathbf{u}}$ ,  ${}^{t+\Delta t} \mathbf{f}_{int}$  and  ${}^{t+\Delta t} \mathbf{f}_c$  are coupled which are unknown at time  $t + \Delta t$ , it is a beneficial attempt to use the explicit method [28]. In this part, the velocity verlet algorithm [23] is applied to solve the Eq. (16). The detailed formulations are as follows,

Predicting stage:

$${}^{t+\Delta t} \mathbf{u}^p = {}^t \mathbf{u} + \Delta \mathbf{u} = {}^t \mathbf{u} + \Delta t \dot{\mathbf{u}} + \frac{1}{2} \Delta t^2 \ddot{\mathbf{u}}, \tag{17}$$

$${}^{t+\Delta t} \dot{\mathbf{u}}^p = {}^t \dot{\mathbf{u}} + \frac{1}{2} \Delta t \ddot{\mathbf{u}}, \tag{18}$$

**Fig. 9** **a** Discrete element discretized into finite elements, and **b** the contact finite elements defined in this case

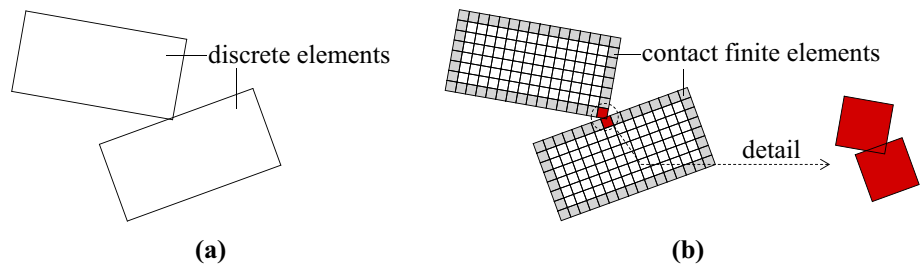
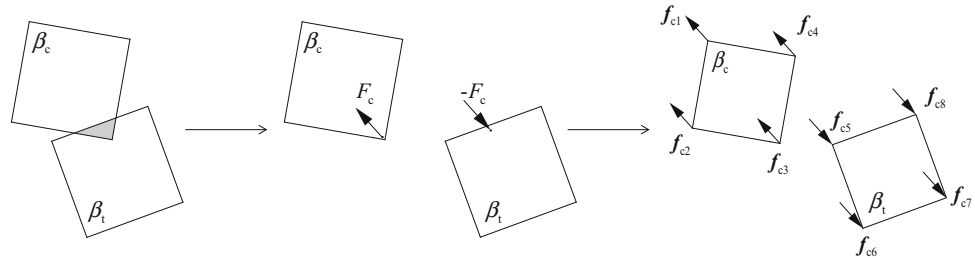


**Fig. 10** Calculation of the equivalent nodal force



Correcting stage:

$${}^{t+\Delta t} \mathbf{u} = {}^{t+\Delta t} \mathbf{u}^p, \tag{19}$$

$${}^{t+\Delta t} \dot{\mathbf{u}} = {}^{t+\Delta t} \dot{\mathbf{u}}^p + \frac{1}{2} \Delta t {}^{t+\Delta t} \ddot{\mathbf{u}}. \tag{20}$$

During this stage, the displacement and the new positions of the nodes at time  $t + \Delta t$  are calculated according to Eq. (17), and the velocity at mid-step is determined by using Eq. (18) [23]. Accordingly, the equivalent nodal force vector of the contact force  ${}^{t+\Delta t} \mathbf{f}_c$  can be compute according to Eqs. (8) (14) and (15). And the internal force vector  ${}^{t+\Delta t} \mathbf{f}_{int}$  related to the configuration is met [27, 29]

$${}^{t+\Delta t} \mathbf{f}_{int} = \int_{0\Omega_e} \mathbf{B}_0^T ({}^t \mathbf{S} + \Delta \mathbf{S})^0 d\Omega \tag{21}$$

or

$${}^{t+\Delta t} \mathbf{f}_{int} = \int_{t\Omega_e} \mathbf{B}_t^T ({}^t \boldsymbol{\tau} + \Delta \mathbf{S})^t d\Omega, \tag{22}$$

where  $\mathbf{B}_0$  and  $\mathbf{B}_t$  are the strain–displacement matrix corresponding to the configurations at time 0 and  $t$ , respectively,  ${}^t \mathbf{S}$  and  ${}^t \boldsymbol{\tau}$  are the matrixes of 2nd Piola–Kirchhoff stress and Cauchy stress at time  $t$ , respectively, and  $\Delta \mathbf{S}$  is the incremental 2nd Piola–Kirchhoff stress related to the incremental displacement  $\Delta \mathbf{u}$ .

The recursion equations of Eq. (16) can be concluded as

$$\mathbf{M}^{t+\Delta t} \ddot{\mathbf{u}} = {}^{t+\Delta t} \mathbf{f}_{ext} + {}^{t+\Delta t} \mathbf{f}_c - \mathbf{C}^{t+\Delta t} \dot{\mathbf{u}}^p + {}^{t+\Delta t} \mathbf{f}_{int}. \tag{23}$$

Finally, the acceleration at time  $t + \Delta t$  is solved according to Eq. (23), and the velocity move completed using Eq. (20).

In this work, it is based on a dynamic algorithm that solves the equations of the motion of the block system through an explicit scheme, and the stiffness matrix does not need to be generated in the solving process. In order to clarify the implementation process of this method, the technical scheme is presented in Fig. 11.

## 5 Verification and application

In this section, several numerical cases are presented to verify the correction and accuracy of the proposed method. Firstly, the superiority of the presented method in capturing the normal and tangential contact forces is illustrated by two standard problems, including the impact simulation and the sliding test. Afterwards, the ability of reflecting the strain and stress fields for each discrete block is proved by discussing the dynamic response of a beam subjected to the impact loading and the instant stress inside the irregular multi bodies in contact. Finally, the verified method is applied to simulate the hopper flow.

### 5.1 Impact simulation between triangular elements

The presented method provides an accurate contact force. To verify this assertion, a benchmark concerning the impact procedure of two triangular blocks is studied. In this example, the rigid block is assumed, due to an intuitive interpretation for the contact force. The models used herein are shown in Fig. 12. Two kinds of models are exhibited here, including the perfectly and incompletely symmetrical triangular couples,  $\beta_c$  and  $\beta_t$  denoted as the case 1, and  $\beta_c$  and  $\beta'_t$  denoted as the case 2, respectively. The blocks are arranged vertically along the Y axis. The blocks  $\beta_t$  and  $\beta'_t$  are fixed, while the



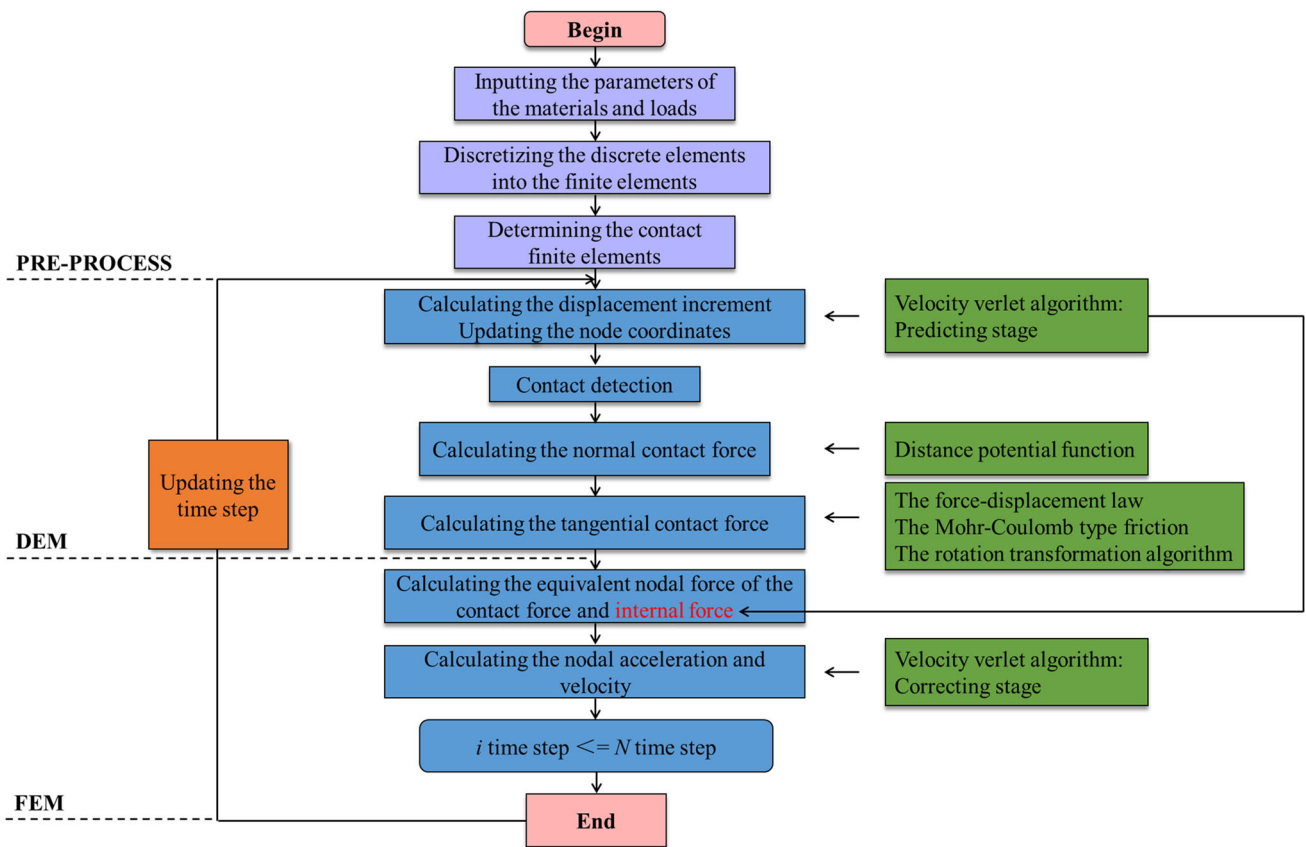


Fig. 11 The technical scheme of the proposed method

block  $\beta_c$  falls toward  $\beta_t$  and  $\beta'_t$  along the Y axis, respectively. The density of blocks is  $2000 \text{ kg/m}^3$  and the initial velocity of block  $\beta_c$  is set as  $0 \text{ m/s}$ . The vertical acceleration due to the gravity is taken to be  $9.81 \text{ m/s}^2$  in a direction opposite that of the Y axis. The normal stiffness,  $k_n = 20 \text{ GPa}$  is considered. Influences of the friction and energy degradation are neglected.

Initially, block  $\beta_c$  free falls toward  $\beta_t$ . When  $\beta_c$  begins to contact with  $\beta_t$ ,  $\beta_c$  gradually decreases its velocity to a standstill following the increment of the penetration. Meanwhile, the embedded area and the normal contact force achieve the maximum value. Then block  $\beta_c$  turns around and returns to the initial position ultimately. The vertical and horizontal displacements of  $\beta_c$  by the proposed method are shown in Figs. 13 and 14, respectively. The simulation with the proposed method follows the expected motion. The main reason is owing to the symmetrical geometric construction of the contact area respect to the Y axis, same physical parameters, and more importantly the same contact forces on  $\Gamma_1$  and  $\Gamma_2$  caused by the penetration, as illustrated in Fig. 15.

The results also exhibit that the movement behavior of  $\beta_c$  is consistent with the existing analysis in the case 2. The vertical displacement of  $\beta_c$ , shown in Fig. 13, is symmetrical along the Y axis, as the identical penetrations between

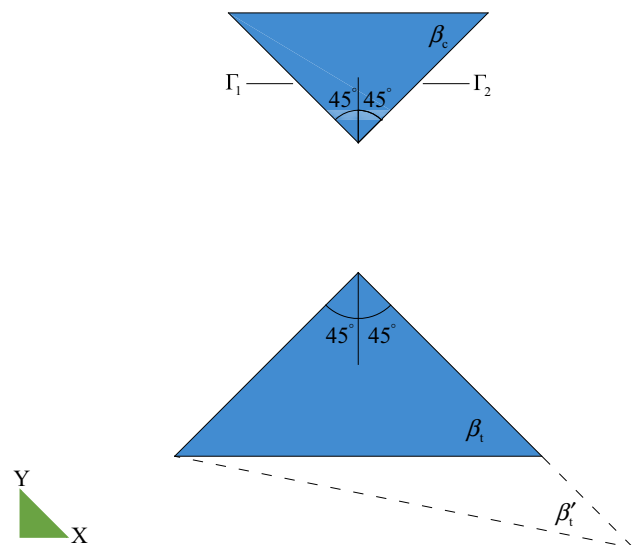
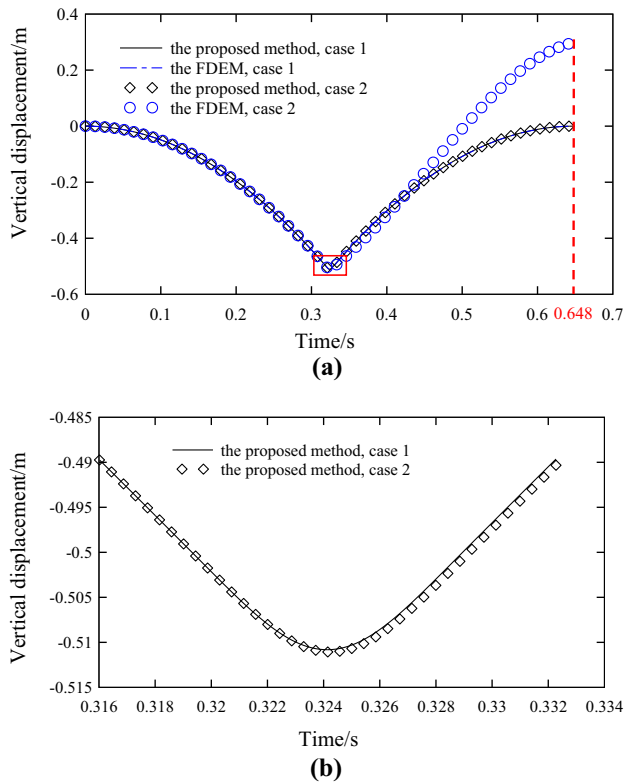
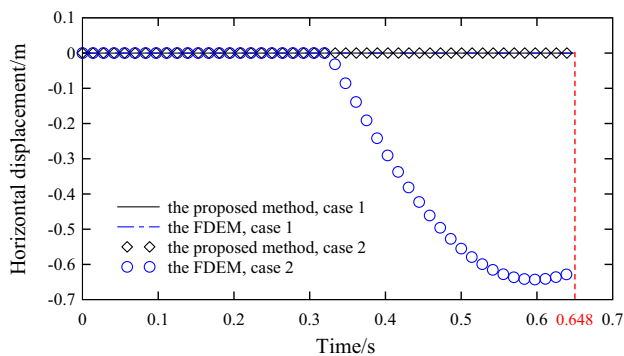


Fig. 12 Numerical models for this impact simulation

the contact blocks in the right and left side. Besides, the displacement along the X axis is not generated, due to the load distribution. These observations indicate that the defined distance potential function is a signed distance function. Thus, both the distance potential value and the contact force inside



**Fig. 13** Simulation results by the proposed method and the FDEM for the impact cases, where **a** the vertical displacement of block  $\beta_c$ , and **b** the detailed time evolution of the displacement of block  $\beta_c$  by the proposed method



**Fig. 14** Time evolution of the horizontal displacement of  $\beta_c$  calculated by the proposed method and the FDEM

an element are calculated without influence of the element shape. In Fig. 15 the difference of the contact forces by using the proposed method between the two cases is shown. This is due to the change of the element shape. For the different blocks, the embeddedness is quite different with each other, even though the same penetration distance is assumed. Thus, it is seen that a slight deviation of the vertical displacements of  $\beta_c$  obtained by the proposed method is generated as shown in Fig. 13b.

As a comparison, the tests with the same setting are also conducted by using the FDEM. The results are presented in Figs. 13a and 14. It is clearly that the motion trajectory is the same before and after the collision in the case 1, however, it shows the opposite result in Fig. 13 for the case 2, and the horizontal movement of  $\beta_c$  is observed during the simulation. As explained in Sect. 2.2, the normal contact forces on  $\Gamma_1$  and  $\Gamma_2$  are unequal with each other, and they result in a horizontal deflection of  $\beta_c$  after it impacts with  $\beta'_t$ . The discrepancy caused by element shape can be observed clearly.

## 5.2 Friction test

In this section, the processes of a block sliding on an inclined surface with an initial velocity and the recording of the rebound trajectory of the triangular block are analyzed as benchmark tests of a friction problem for this proposed method.

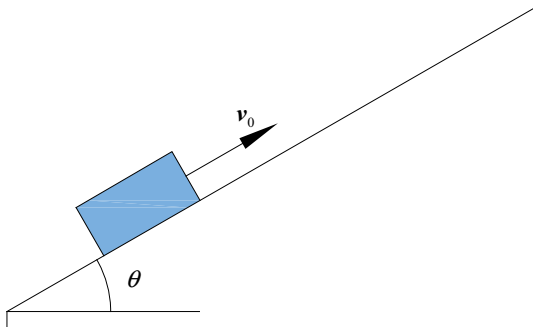
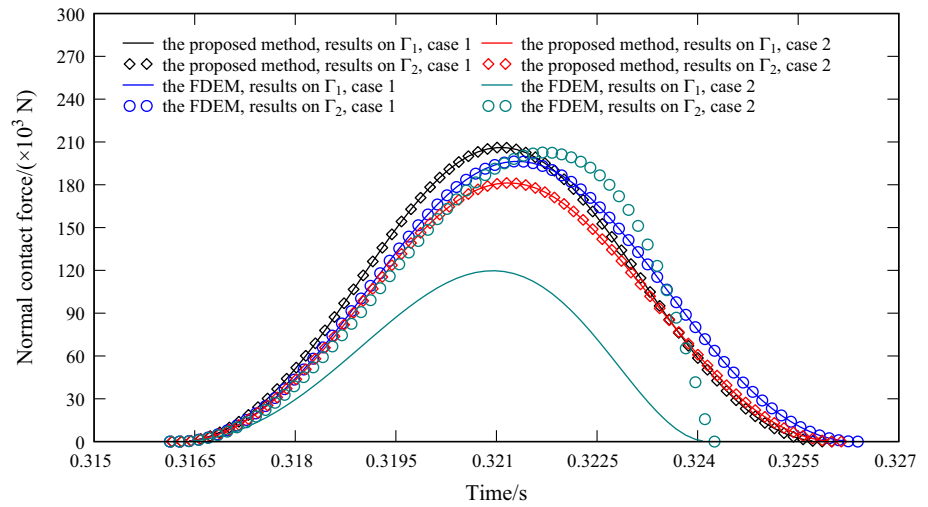
The simplified physical model applied in the first friction test is shown in Fig. 16. In the beginning, the block is placed on the inclined surface with a dip angle  $\theta = 30^\circ$ . The initial velocity of the sliding block is set as 6 m/s. The density of the block is  $2500 \text{ kg/m}^3$ . The normal stiffness,  $k_n = 2.0 \text{ GPa}$ , and the tangential stiffness,  $k_s = 1.25 \text{ GPa}$ , are assigned to the blocks. Various friction coefficients  $\mu = 0.2, 0.4, 0.6$ , are implemented to set up the slide path artificially. The simulation results are compared with the theoretical value.

Figure 17 shows the velocity and displacement of the sliding block. The results exhibit an explicit conversion procedure of the kinetic energy of the block with different frictional coefficients. In this detailed description of a comprehensive test, it is seen that results calculated by the proposed method agree well with the theoretical values.

The following simulation provides a comparison between the proposed method and the developed method by Yan [20]. As shown in Fig. 18,  $\beta_t$  is fixed on the ground and  $\beta_c$  falls toward  $\beta_t$  driven by the gravity. The physical properties of the blocks are the same, which the density are  $2000 \text{ kg/m}^3$ , the normal stiffness is 2.0 GPa, and the tangential stiffness,  $k_s = 1.25 \text{ GPa}$ , is used here. The initial velocity of  $\beta_c$  is set as 0 m/s. The friction coefficient,  $\mu = 0.1$ , is assumed.

As the relative tangential displacement between the blocks  $\beta_c$  and  $\beta_t$  is not occurred during the movement process,  $\beta_c$  turns into a reverse motion and ultimately returns the original position after impacts with block  $\beta_t$ , due to the moving power without losing energy. As a result, tangential forces and the energy loss caused by the tangential forces are not included in this case. Figure 19 presents the displacement of  $\beta_c$ . It is worthwhile to notice that the displacement of  $\beta_c$  obtained by the proposed method maintains a constant amplitude, while its peak value decreases gradually simulated with the developed method by Yan, as shown in Fig. 20, due to

**Fig. 15** Normal contact forces on  $\Gamma_1$  and  $\Gamma_2$  obtained by two methods for the impact cases



**Fig. 16** Numerical model for the sliding test

losing energy caused by the false tangential force by Eq. (8), as exhibited in Fig. 21.

Based on above discussion, the precision of the tangential contact force by the proposed method is deduced.

### 5.3 The vibration tests for the beam under the impact load

The vibration test cases for the cantilever and the statically indeterminate beam responding the dynamic load [30] are simulated to verify the accuracy of the proposed method in solving the problem in the context of elasticity.

The first case is now presented in this section to investigate vibration procedure of the cantilever beam subjected to the impact load. The test beam is with a length of 10 m and a height of 1 m, as shown in Fig. 22. The load is placed 0.2 m apart from the right side of the beam, whose maximum is  $1.5 \times 10^7$  N, and the rise time,  $t_0 = 0.5$  s, is assigned, shown in Fig. 23. The density of the beam is  $2000 \text{ kg/m}^3$ , the Young's modulus is 20 GPa, and the Poisson's ratio is set as 0.2. Influence of the element size is also considered in this case and the calculated model is discretized into structured

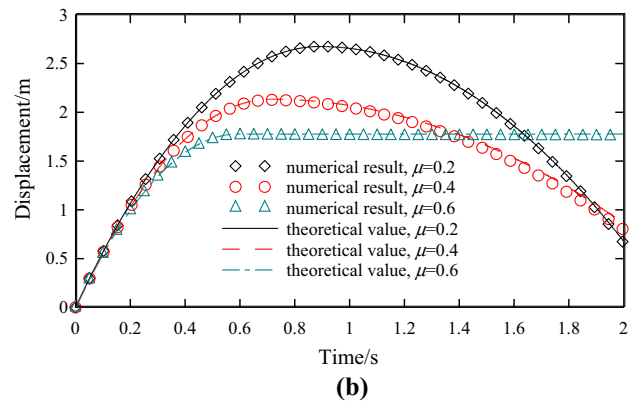
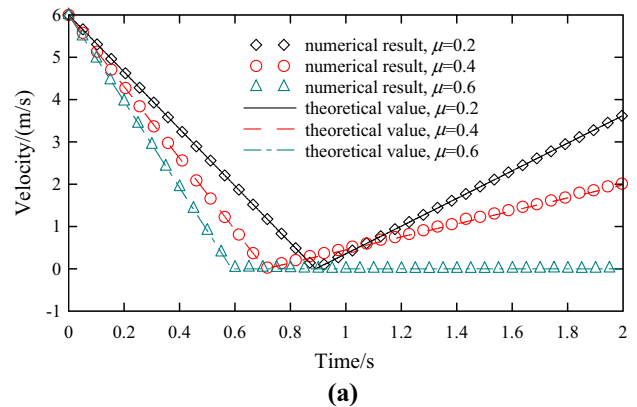


**Fig. 17** Velocities and displacements obtained by **a** the proposed method and **b** the theoretical equations

quadrilateral elements of the size 0.05 m, 0.1 m, and 0.2 m, respectively.

For a comparison, the simulation is also pursued by ADINA. The deflection at point A is shown in Fig. 24. It illustrates that the simulation results obtained by the proposed method with different element sizes are in good agreement

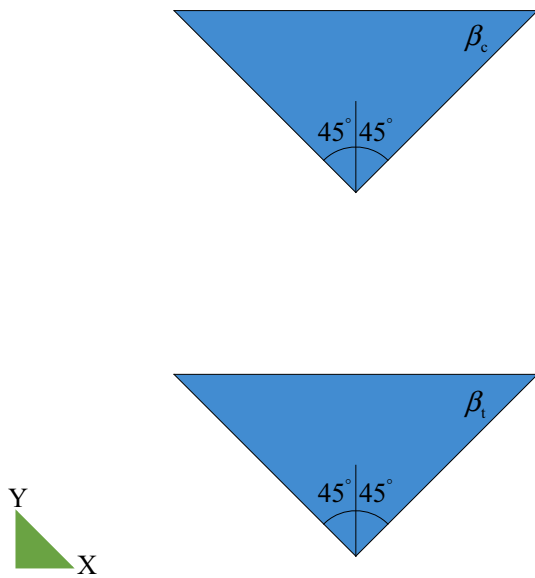


**Fig. 18** Numerical model consisted of two triangular blocks

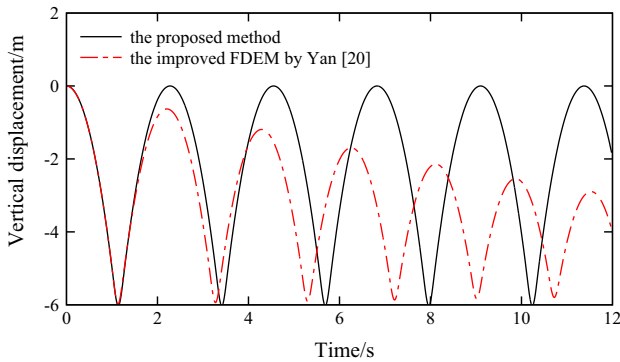


**Fig. 19** Vertical displacement obtained by the proposed method and the improved FDEM by Yan [20]

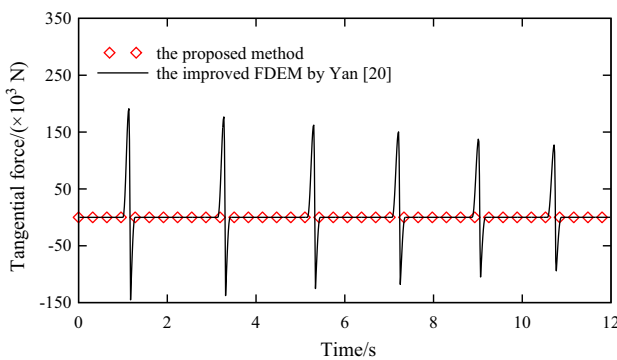


**Fig. 20** Time evolution of the tangential fore obtained by the two methods

with that calculated by ADINA, when the element is small enough.

The following simulation is performed to validate the capability of the proposed method to capture the deformation

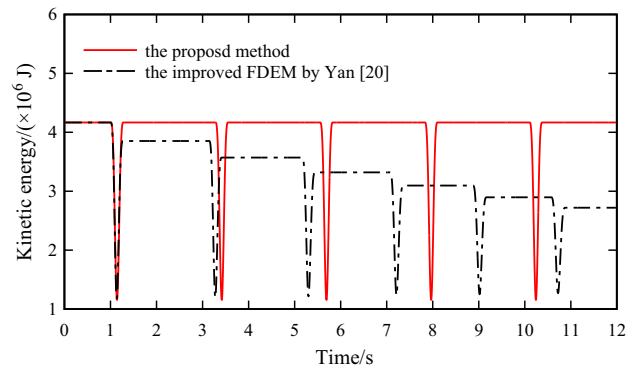


**Fig. 21** Kinetic energy as a function of time calculated by the two methods

behavior and prediction stress inside the individual block. The tested beam model is constructed with 1000 quadrilateral finite elements with the size  $0.1 \text{ m} \times 0.1 \text{ m}$ , namely (span  $\times$  high) as shown in Fig. 25. The material properties are same with the description in the first case. The initial velocity of the projectile is set as  $-1 \text{ m/s}$ . The impactor is just on the top of the beam. Initially, they are stacked in such way that they contact, but there are no overlap and contact force between them. The test with the same setting is also simulated by ADINA.

The results are presented in Figs. 26 and 27. The curve at the point A obtained by the proposed method is almost coincident with that by ADINA. Figure 28 presents the major principal stress  $\sigma_1$  of the beam at about  $0.7 \text{ ms}$  and  $1.5 \text{ ms}$ , respectively. The stress distributions simulated by the two methods are similar with each other. Thus, the accuracy of the newly presented method in this work is further proved.

### 5.4 Multi-bodies contacting test

This section provides the results of a study, carried out by the proposed method, on the plane Hertzian contact stress between two cylinders, as shown in Fig. 29. The results are compared, following the analysis, to the calculated stress based on Hertz's theory (1881–1882). The cylinder body  $\beta_I$  of radius  $R_1$  in contact with  $\beta_{II}$ , is compressed with a uniformly distributed force  $F$ . In contact between the cylinders, the contact force is linearly proportional to the indentation depth [31]. The half-width  $b$  of the contact area is obtained as

$$b = \sqrt{\frac{4F \left[ \frac{1-\nu_1^2}{E_1} + \frac{1-\nu_2^2}{E_2} \right]}{\pi L \left( \frac{1}{R_1} + \frac{1}{R_2} \right)}}, \tag{24}$$

where  $E_1$  and  $E_2$  are the elasticity modulus of cylinders  $\beta_I$  and  $\beta_{II}$ , respectively,  $\nu_1$  and  $\nu_2$  represent the Poisson's ratios, and  $L$  is the length of contact.

**Fig. 22** The cantilever beam model subjected to impact load

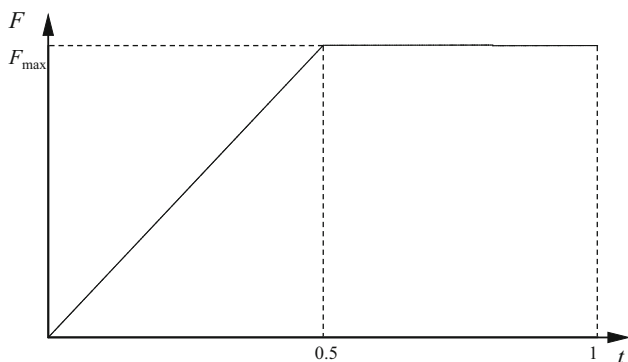
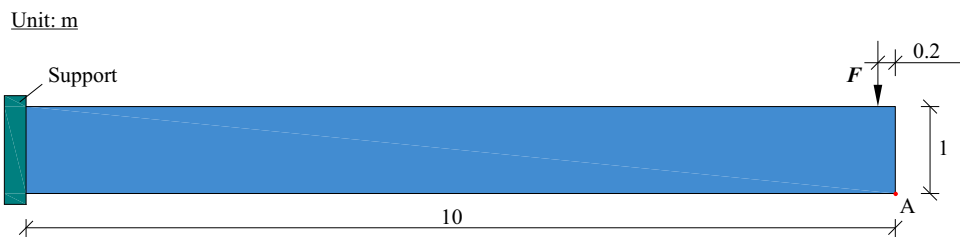


**Fig. 23** The impact load acting on the beam

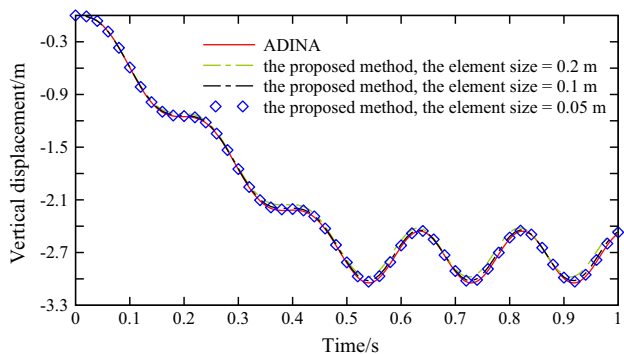


**Fig. 24** Deflection at point A for several element sizes

Therefore, the maximum contact pressure  $p_{max}$  along can be achieved as follows

$$p_{max} = \frac{2F}{\pi bL}. \tag{25}$$

The analytical model is realized considering a plane perpendicular on the cylinder axis as shown in Fig. 30. The model is discretized into 8776 finite elements. The size of

**Fig. 25** Element configuration of the tested beam

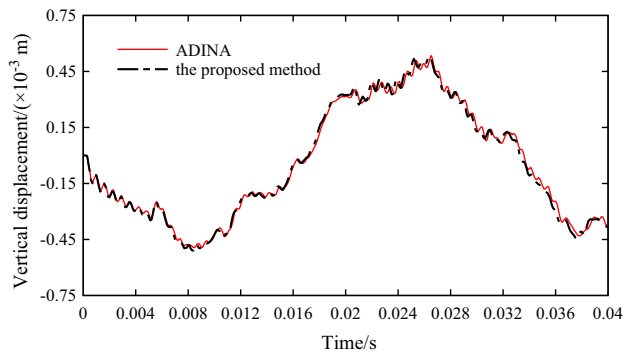
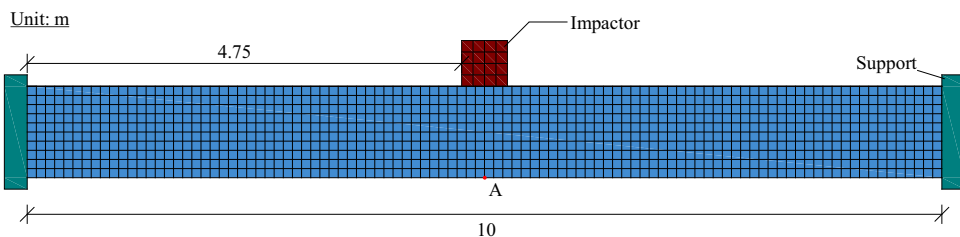


**Fig. 26** Time evaluation of the vertical displacement at the point A obtained by the two methods

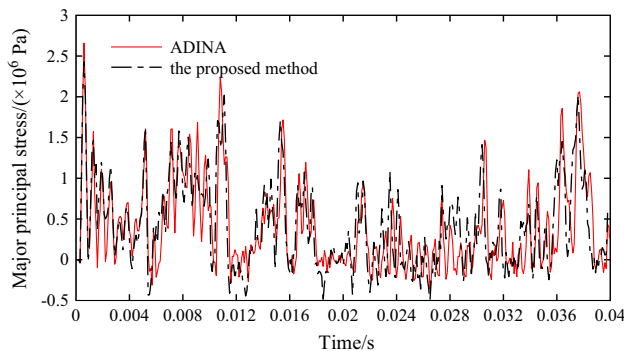


**Fig. 27** Comparison of the major principal stress at point A

coarse mesh utilized is 0.02 m, whereas the fine mesh is  $1 \times 10^{-4}$  m. The mechanical properties of the materials are  $E_1 = E_2 = 20$  GPa and  $\nu_1 = \nu_2 = 0.21$ . The normal load  $F = 1 \times 10^8$  N and unit length of contact are applied. The contact stiffness used in this case is  $k_n = 20$  GPa. Influence of gravity and friction are not included. Therefore, the maximum contact pressure according to Eq. (25),  $p_{max} = 3.87101 \times 10^9$  Pa, can be obtained.



**Fig. 28** Snapshots of major principal stress at **a**  $t = 0.7$  ms and **b**  $t = 1.5$  ms

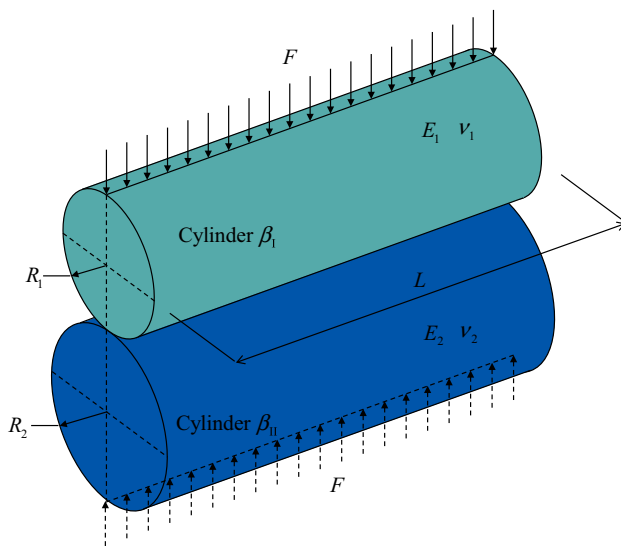
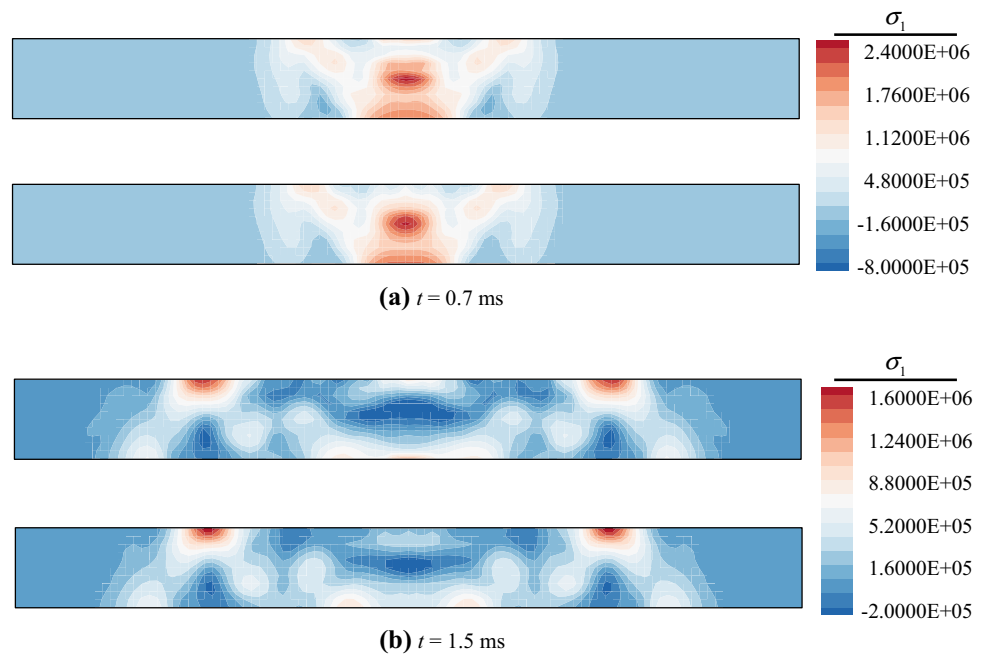


**Fig. 29** Model of the contact cylinders

The simulation results are presented in Fig. 31. It worthwhile to notice that the distribution of the displacement and minor principle stress fields  $\sigma_{\min}$  are symmetrical to the direction of the force and the contact point. The maximum of the stress is in the contact point, which agrees well with the theoretical value calculated according to Eq. (25).

The following simulation is on the basis of the uniaxial compression test, consisted of disks and irregular blocks, to demonstrate the proposed method in dealing with the multi-

bodies system under compression. Quite evidently the stress is consistent with the Hertz's equation for the simplified case. However, for the cases including a larger number of contacts, as shown in Fig. 32, the stress is not simple enough to be represented by the universal formula [32].

This test is performed by the proposed method. The stress states of the blocks are presented in Fig. 32. The stress fields exhibit strong heterogeneity and are varying with the contact conditions. When they contact with each other, significant stress concentrations appear in the contact point. The disappearance of the contact force and the stress field can be observed, if they are separated from each other. It further demonstrates the capability of the developed method in capturing the conditions in the process of contact.

## 5.5 Simulation of the hopper flow

In this section, the proposed method is introduced to an application of the study of the jamming phenomenon of granular flow. This simulation is pursued on the basis of the investigation of Galindo-Torres [33]. It has been demonstrated that the particles may become jammed, when the opening is smaller than a critical value, and the nonconvex particles are expected to jam more easily than convex particles [34].

In the framework of current simulation, the geometry of the hopper is shown in Fig. 33. The test is carried out using the quadrilateral and cross-shaped blocks. All the blocks are considered as rigid blocks. The density of the blocks is

**Fig. 30** Modeling and meshing contact between the two cylinders with parallel axes

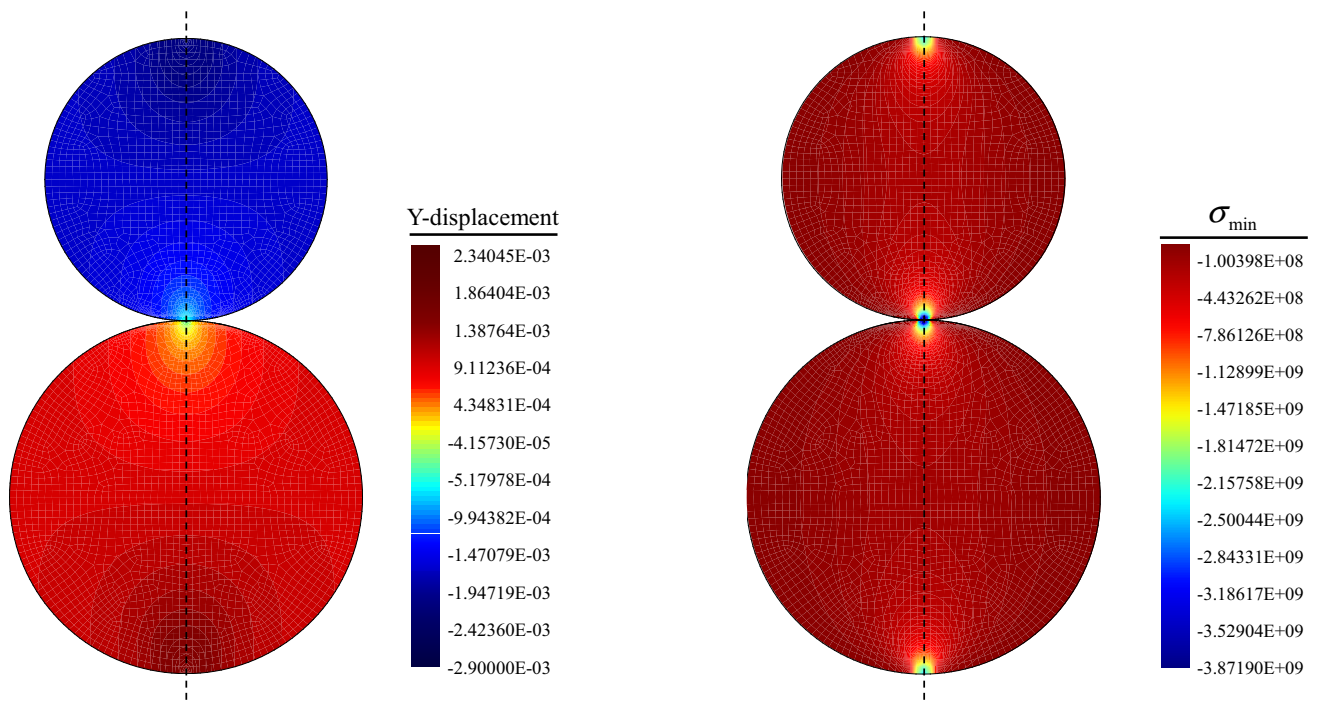
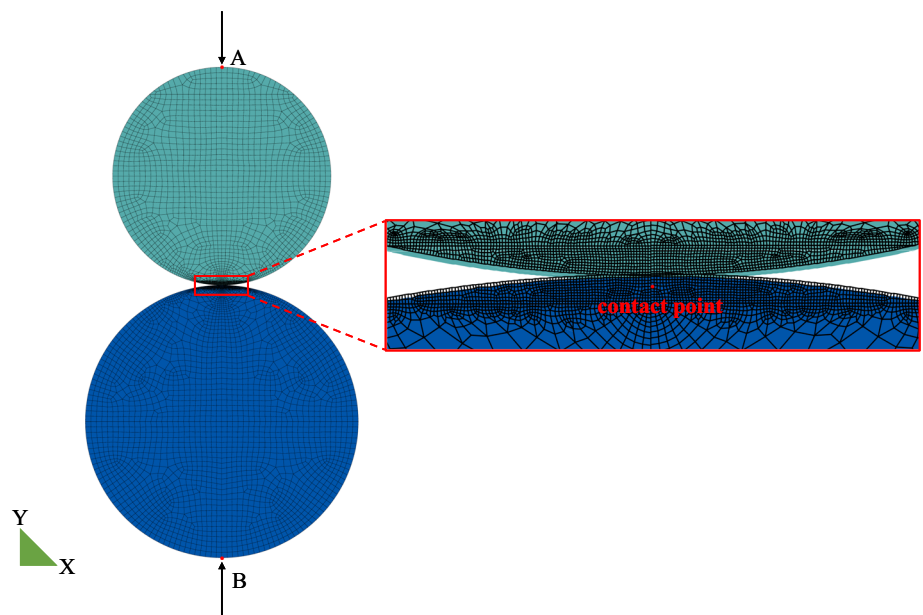


**Fig. 31** The vertical displacement and the minor principal stress fields obtained by the proposed method

assumed as  $2000 \text{ kg/m}^3$ . The normal stiffness  $k_n = 2.0 \text{ GPa}$  and damping coefficient  $0.0005$  are applied. The influence of friction between the blocks and wall is neglected. Blocks are assigned a random arrangement in hopper and driven by the gravity. The snapshots on the discharge processes for the differently shaped blocks are shown in Fig. 34. It should be

note that the opening is large enough and the quadrilateral blocks can free fall from the hopper, while the jamming of the cross-shaped blocks is produced by arches formed near the aperture.

Simulations are also carried out to explore the influence of the elasticity modulus. The blocks are assigned value of

**Fig. 32** Stress field inside the contact blocks, where **a**  $\sigma_{xx}$ , **b**  $\sigma_{yy}$ , and **c**  $\sigma_{xy}$

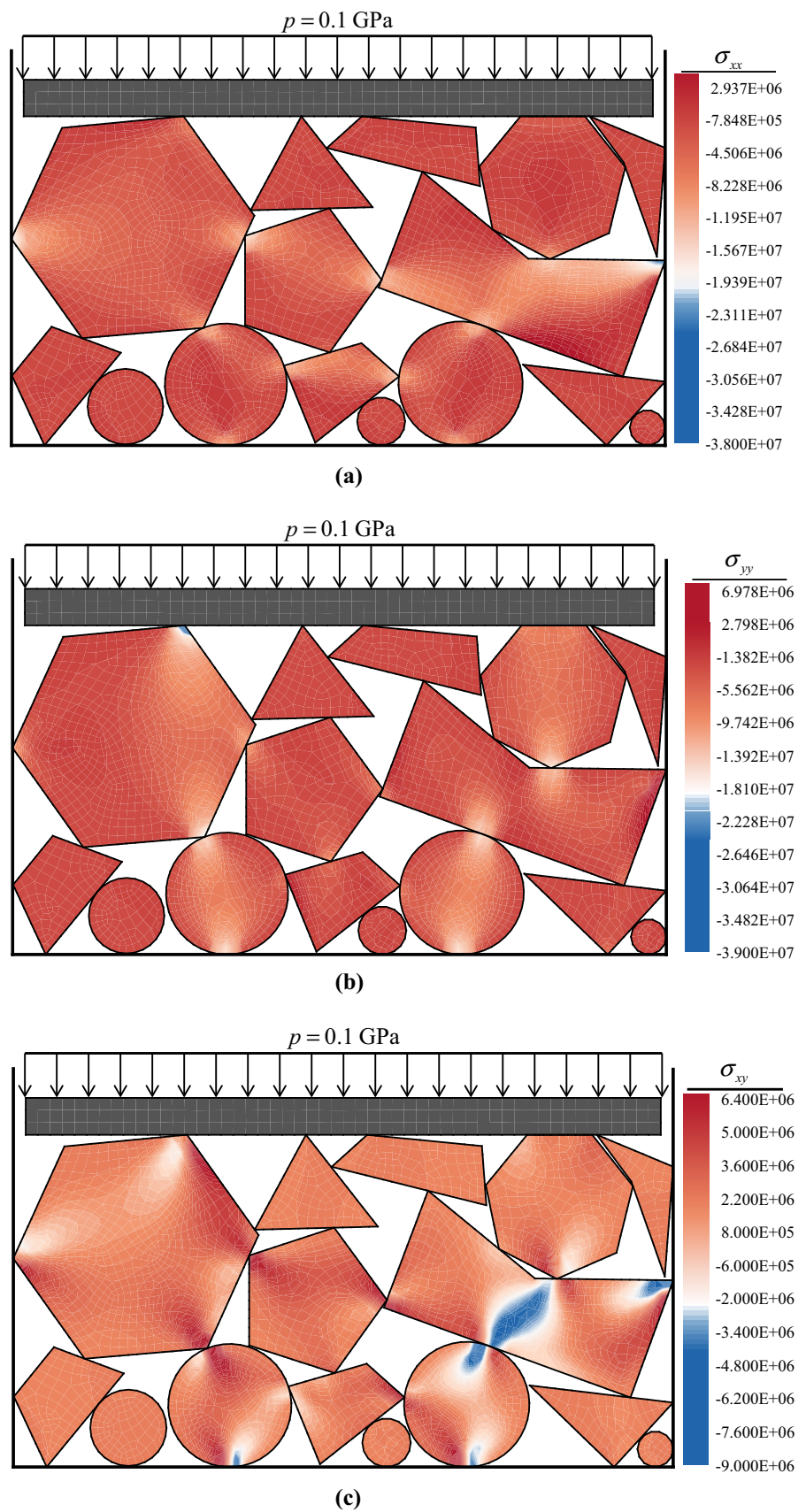


**Fig. 33** Geometry properties of the model used in this example

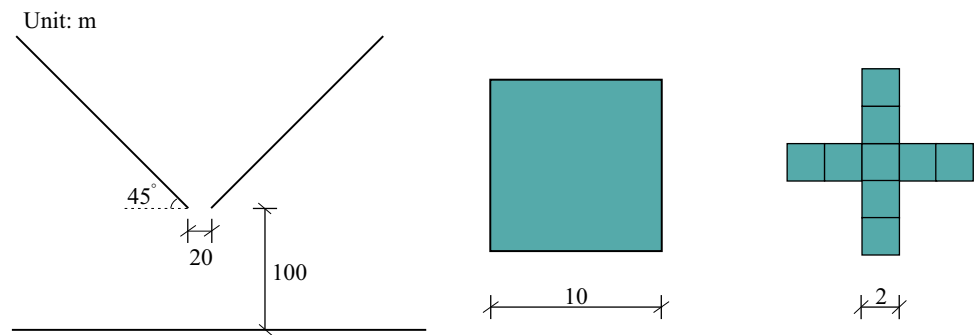
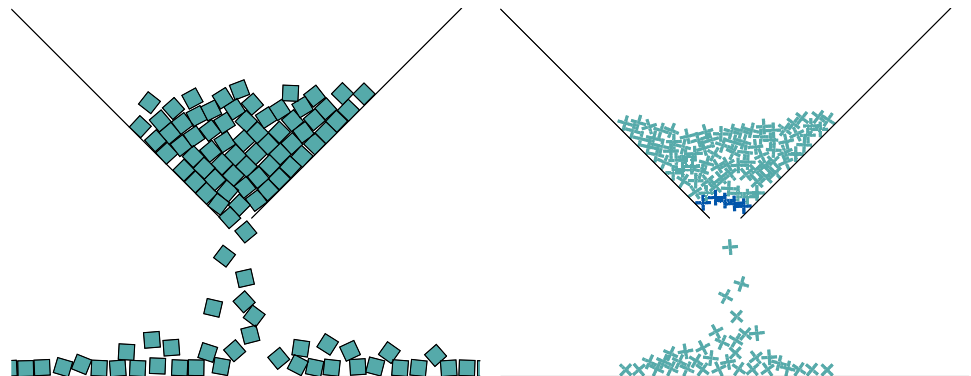


**Fig. 34** Simulation of the hopper flow using the rigid structured quadrilateral blocks and cross-shaped blocks by the proposed method



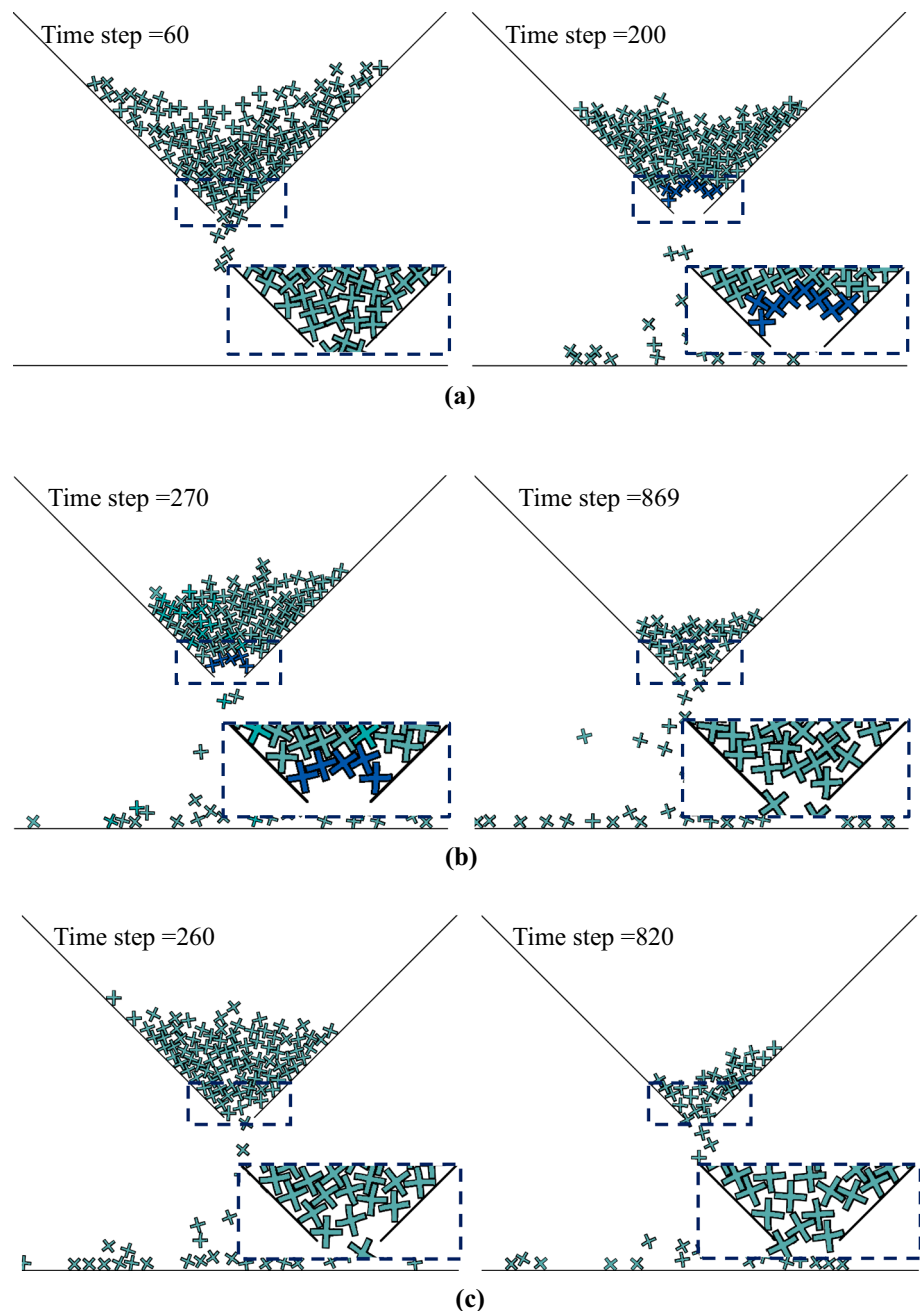
Young's modulus of 1.2 GPa, 0.5 GPa, and 0.3 GPa, respectively, and the Poisson's ratio 0.2. The detail description of the simulation results is shown in Fig. 35. The state of the rest illustrates variation of the behavior of the discharge flow. In the instance  $E = 2.4$  GPa, the deformation is not significantly and the jamming is still produced formed near the aperture, as illustrated in Fig. 35a. For the case shown in Fig. 35b, the flow is jammed after few blocks discharged, whereafter, the emptying process of the hopper for the blocks are observed, due to the loss of the stability of the arch caused by the excessive deformation of the blocks. As exhibited in Fig. 35c, emptying process presents that the jamming is not generated, when the elasticity modulus is small enough. It is seen that the deformation characteristics of the blocks plays a critical role in the macroscopic flow behavior and the proposed method is a powerful tool to model the behavior of the particle flows consisted of multiple deformable bodies.

## 6 Conclusions

The main challenges in simulating the motion of the system consisted of multiple deformable bodies include the repre-

sentation of the contact interactions and the description of the stress and strain fields inside the individual blocks. In the current work, a novel distance potential function-based FEM-DEM method is proposed. The newly presented method has constructed a basic function of the distance potential function, and a complete normal contact force calculation model, including the magnitude and the direction. For simulating the sliding procedure of the discontinuous system, a fundamental algorithm of the tangential contact force is developed in detail relying on the displacement increment method and the classical Mohr–Coulomb type friction algorithm by coupling the rotation transformation algorithm. With the conversion method of the equivalent nodal force, the calculated contact forces are applied together with other nodal forces in order to generate the corresponding equations of motion. The velocity verlet algorithm is adopted to simplify the calculation of the equations of motion and update the strain and stress fields at each time step. Compared with the FDEM, the contact forces are calculated regardless of the element shape, and the stress and strain fields are with high precise, due to much wider range of choices for element types. The advantages of the proposed method are verified by some benchmark examples. The results show that this computational method is clear, precise, and stable for 2D models.

**Fig. 35** Simulation of the hopper flow using the deformable blocks for several elasticity modulus, where **a**  $E = 2.4$  GPa, **b**  $E = 0.5$  GPa, and **c**  $E = 0.3$  GPa



**Acknowledgements** This work is supported by the National Key R&D Program of China (Grant 2018YFC0406705), China Postdoctoral Science Foundation Funded Project (Grant 2019M651677), the 15th Fok Ying-Tong Education Foundation for Young Teachers in the Higher Education Institutions of China (Grant 151073), the Priority Academic Program Development of Jiangsu Higher Education Institutions (Grant YS11001), the 111 Project and Qing Lan Project.

## References

1. Tang XH, Paluszny A, Zimmerman RW (2014) An impulse-based energy tracking method for collision resolution. *Comput Methods Appl Mech Eng* 278:160–185
2. Chen LP, Li XJ, Zhang YH, Chen TW, Xiao SY, Liang HJ (2018) Morphological and mechanical determinants of cellular uptake of deformable nanoparticles. *Nanoscale* 10:11969–11979
3. Cundall PA, Strack ODL (1979) A discrete numerical model for granular assemblies. *Géotechnique* 29:47–65
4. Cundall PA (1988) Formulation of a three-dimensional distinct element model—part I. A scheme to detect and represent contacts in a system composed of many polyhedral blocks. *Int J Rock Mech Min Sci Geomech Abstracts* 25:107–116
5. Hart R, Cundall PA, Lemos J (1988) Formulation of a three-dimensional distinct element model—part II. Mechanical calculations for motion and interaction of a system composed of many polyhedral blocks. *Int J Rock Mech Min Sci Geomech Abstracts* 25:117–125



6. Smoljanovic H, Zivaljic N, Nikolic Z, Munjiza A (2018) Numerical analysis of 3D dry-stone masonry structures by combined finite-discrete element method. *Int J Solids Struct* 136:150–167
7. Zhao LH, Liu XN, Mao J, Xu D, Munjiza A, Avital E (2018) A novel contact algorithm based on a distance potential function for the 3D discrete-element method. *Rock Mech Rock Eng* 51:3737–3769
8. Zhao LH, Liu XN, Mao J, Shao LY, Li TC (2020) Three-dimensional distance potential discrete element method for the numerical simulation of landslides. *Landslides* 17:361–377
9. Bao HR, Zhao ZY (2012) The vertex-to-vertex contact analysis in the two-dimensional discontinuous deformation analysis. *Adv Eng Softw* 45:1–10
10. Munjiza A, Owen DRJ (1995) A combined finite-discrete element method in transient dynamics of fracturing solids. *Int J Eng Comput* 12:145–174
11. Munjiza A, Andrews KRF (1998) NBS contact detection algorithm for bodies of similar size. *Int J Numer Methods Eng* 43:131–149
12. Munjiza A (2004) *The combined finite-discrete element method*. Wiley, Chichester
13. Smoljanovic H, Nikolic Z, Zivaljic N (2015) A finite-discrete element model for dry stone masonry structures strengthened with steel clamps and bolts. *Eng Struct* 90:117–129
14. Barla M, Piovano G, Grasselli G (2012) Rock slide simulation with the combined finite-discrete element method. *Int J Geomech* 12:711–721
15. Vyazmensky A, Stead D, Elmo D, Moss A (2010) Numerical analysis of block caving-induced instability in large open pit slopes: a finite element/discrete element approach. *Rock Mech Rock Eng* 43:21–39
16. Fathani TF, Karnawati D, Wilopo W (2016) An integrated methodology to develop a standard for landslide early warning systems. *Nat Hazard Earth Sys* 16:2123–2135
17. Mao J, Zhao LH, Di YT, Liu XN, Xu WY (2020) A resolved CFD-DEM approach for the simulation of landslides and impulse waves. *Comput Methods Appl Mech Eng* 359
18. Mao J, Zhao LH, Liu XN, Avital E (2020) A resolved CFDEM method for the interaction between the fluid and the discontinuous solids with large movement. *Int J Numer Meth Eng* 121:1738–1761
19. Zhao LH, Liu XN, Mao J, Xu D, Munjiza A, Avital E (2018) A novel discrete element method based on the distance potential for arbitrary 2D convex elements. *Int J Numer Methods Eng* 115:238–267
20. Yan CZ, Zheng H (2017) A new potential function for the calculation of contact forces in the combined finite-discrete element method. *Int J Numer Anal Meth Geomech* 41:265–283
21. Xiang J, Munjiza A, Latham J (2009) Finite strain, finite rotation quadratic tetrahedral element for the combined finite–discrete element method. *Int J Numer Methods Eng* 79:946–978
22. Dasgupta G (2003) Interpolants within convex polygons: wachspress’ shape functions. *J Aerospace Eng* 16:1–8
23. Allen MP, Tildesley DJ (1987) *Computer simulation of liquids*. Oxford University Press, Oxford
24. Euser B, Rougier E, Zhou L, Knight EE, Frash LP, Carey JW, Viswanathan H, Munjiza A (2019) Simulation of fracture coalescence in granite via the combined finite–discrete element method. *Rock Mech Rock Eng* 52:3213–3227
25. Feng YT, Han K, Owen DRJ (2012) Energy-conserving contact interaction models for arbitrarily shaped discrete elements. *Comput Methods Appl Mech Eng* 205:169–177
26. Zienkiewicz OC, Taylor RL, Zhu JZ (2005) *The finite element method: its basis and fundamentals*. Elsevier Butterworth-Heinemann, Amsterdam
27. Munjiza A, Rougier E, Knight EE (2015) *Large strain finite element method: a practical course*. Wiley, Chichester
28. Komodromos P (2005) A simplified updated Lagrangian approach for combining discrete and finite element methods. *Comput Mech* 35:305–313
29. Bathe K, Ramm E, Wilson EL (1975) Finite element formulations for large deformation dynamic analysis. *Int J Numer Methods Eng* 9:353–386
30. Xu W, Zang MY (2014) Four-point combined DE/FE algorithm for brittle fracture analysis of laminated glass. *Int J Solids Struct* 51:1890–1900
31. Brezeanu LC (2015) Contact stresses between two cylindrical bodies: cylinder and cylindrical cavity with parallel axes—part I: theory and FEA 3D modeling. *Procedia Technol* 19:169–176
32. Jiang Y, Herrmann HJ, Alonsomarroquin F (2018) A boundary-spheropolygon element method for stress determination and breakage modelling of particles. *arXiv: Soft Condensed Matter* (2018)
33. Galindo-Torres SA, Alonso-Marroquin F, Wang YC, Pedrosa D, Castano JDM (2009) Molecular dynamics simulation of complex particles in three dimensions and the study of friction due to non-convexity. *Phys Rev E* 79:060301
34. Alonso-Marroquin F (2008) Spheropolygons: a new method to simulate conservative and dissipative interactions between 2D complex-shaped rigid bodies. *Epl-Europhys Lett* 83:14001

**Publisher’s Note** Springer Nature remains neutral with regard to jurisdictional claims in published maps and institutional affiliations.